

## CFD SIMULATION OF MOTION RESPONSES OF A TRIMARAN IN REGULAR HEAD WAVES

(DOI No: 10.3940/rina.ijme.2020.a1.595)

**L Nowruzi**, and **H Enshaei**, Australian Maritime College, University of Tasmania, Australia, **J Lavroff**, School of Engineering, University of Tasmania, Australia, **S S Kianejad**, Australian Maritime College, University of Tasmania, Australia, **M R Davis**, School of Engineering, University of Tasmania, Australia

### SUMMARY

CFD has proved to be an effective method in solving unsteady Reynolds–Averaged Navier-Stokes (RANS) equations for analysing ships in free surface viscous flow. The research reported in this paper is intended to develop a better understanding of the parameters influencing high-speed trimaran motions responses. Variations of gridding system and time step have been investigated and reliability analysis was performed in solving the RANS equations. Different turbulence models were investigated, and the SST Menter K Omega turbulence model proved a more accurate model than Realizable K-epsilon model. In order to validate the CFD method, the results of the motions response of a high-speed trimaran are compared against a set of experimental and numerical results from a 1.6 m trimaran model tested in various head seas conditions. The results suggest that CFD offers a reliable method for predicting pitch and heave motions of trimarans in regular head waves when compared to traditional low speed strip theory methods. Unlike strip theory, the effect of breaking waves, hull shape above waterline and green seas are considered in CFD application. A wave resonance phenomenon was observed and wave deformation as a result of wave-current-wind interaction in CFD was identified as the main source of discrepancy. The results from this work form the basis for future analysis of trimaran motions in oblique seas for developing a better understanding of the parameters influencing the seakeeping response, as well as passenger comfort.

### NOMENCLATURE

$St$	Stagger Ratio (longitudinal position of the outrigger transoms/ hull length) with respect to main hull transom
$Cl$	Clearance Ratio (transverse position of the outriggers from centre line/ hull length)
$A_0$	Wave amplitude (m)
$A_3$	Heave amplitude (m)
$A_5$	Pitch amplitude (radians)
$B_1$	Beam of main hull (m)
$B_2$	Beam of outrigger (m)
$\Delta$	Displacement (kg)
$C_M$	Maximum section coefficient
$C_B$	Block coefficient
$C_P$	Prismatic coefficient
$C_{WP}$	Waterplane area coefficient
$L$	Centre hull waterline length (m)
$L_1$	Centre hull overall length (m)
$L_2$	Outrigger length (m)
$V$	Volume of displacement ( $m^3$ )
$s$	Hull spacing (distance between centre lines of outriggers and main hull) (m)
$V$	Forward velocity (m/sec)
$\Delta_s$	Displacement of the outriggers (kg)
$TF_3$	Heave Transfer Function
$TF_5$	Pitch Transfer Function
$K$	Turbulent Kinetic energy ( $m^2/sec^2$ )
$r$	Longitudinal distance between main hull transom and the outrigger transoms (m)
$B$	Waterline Beam overall (m)
$B_1$	Centre hull waterline beam (m)
$m$	Mass of the hull (kg)
$\delta_{RE_{G1}}^*$	Numerical error given by generalised Richardson extrapolation

$C_G$	Correction factor
$S_3$	Variation of simulation results for coarse mesh
$S_2$	Variation of simulation results for medium mesh
$S_1$	Variation of simulation results for fine mesh
$P_G$	Order of accuracy
$T_i$	Reynolds Stress Tensor
$\mu_t$	Turbulent Viscosity
$U_I$	Uncertainty in iterative convergence
$U_G$	Grid spacing uncertainty
$U_T$	Time step uncertainty
$R_G$	Numerical convergence ratio
$U_{GC}$	Uncertainty
$\delta_{SN}^*$	Numerical error
$r_G$	Grid spacing refinement ratio
$r_T$	Time step refinement ratio
$\omega$	Dissipation rate
$\omega_e^*$	Dimensionless wave encounter frequency
$k$	Kinetic Turbulent Energy
$C_\mu$	realizable time scale coefficient
$T$	Viscous Stress Tensor
$\varepsilon$	Turbulent Dissipation rate
$\rho$	Density
$M$	Tensor of moments of Inertia

### 1. INTRODUCTION

Trimarans consist of a main hull and two side hulls called outriggers. The configuration provides flexibility for a designer in shaping the general arrangement plan. Trimaran concepts have numerous advantages when compared to monohulls and catamarans that have been discussed by previous

researchers (Armstrong and Holden, 2003, Boote et al., 2004, Fach, 2004, Lindstrom et al., 1995). Wang et al. (2011) indicated small wave-making resistance as well as good transverse stability for high-speed trimarans. Pattison and Zhang (1994) were the first to publish a paper on trimaran ships. Since then, many other scholars (Du et al., 2019, Fang and Too, 2006, Ghadimi et al., 2019, Kim et al., 2019, Nowruzi et al., 2019, Wang et al., 2018, Wu et al., 2011) have investigated the trimaran design both numerically and experimentally. However, in terms of motion response there is still a limited understanding, specifically the roll amplitude and accelerations that may occur and this demands further investigation (Jersey Action Group, 2016, JT901, 2015).

At the beginning of the century, roughly 80% of seakeeping computations were conducted by way of low speed strip theory (LSST) methods (Beck et al., 2001). Earlier on, Newman (1979) had proven some inconsistencies in using the conventional strip theories. Faltinsen and Zhao (1991) also questioned the validity of LSST methods when applied at higher speeds. In 1994, the hydrodynamics department of QinetiQ Haslar tested the first frigate trimaran model (Grafton, 2007). Doctors and Scrace (2003) investigated the influence of different parameters on the hydrodynamics of trimarans. Also, Faltinsen et al. (2003) investigated the slamming effect on the wet deck. They concluded that there will be radiated wave interaction between the hulls at lower speeds. Yasukawa (2005), Grafton (2007) and Dobashi (2014) used both linear and non-linear potential flow-based seakeeping theories for predicting the roll motions of trimaran vessels. Onas (2009), used a 6 DoF potential flow Rankine-panel numerical method to study a prototype trimaran vessel. Hebblewhite et al. (2007) studied the motions of a high-speed trimaran in head seas by shifting the outriggers rearward. They analysed the motions by comparing the results using HYDROS, a potential flow-based LSST code against towing tank experimental data.

Most of the previous numerical approaches are limited in terms of considering the effect of viscosity and turbulence. Some of these limited approaches can be addressed by more advanced theories, such as unsteady Reynolds-Averaged Navier-Stokes (RANS) methods (Beck et al., 2001). Tezdogan et al. (2014a) suggested using 3-D techniques to study seakeeping problems on the basis of advancement in computational technology, where effects of breaking waves, turbulence and viscosity (which are not considered in the potential flow-based theories) could be taken into account by RANS (Simonsen et al., 2013). Thus, applications of CFD-based RANS methods are rapidly growing in terms of seakeeping computations (Tezdogan et al., 2014b).

In this research, an advanced 3-D technique has been utilised to study the pitch and heave motions of a trimaran model. The main objective of this study is to investigate the capability of CFD methods by calculation of RANS equations for a high-speed trimaran vessel. A series of simulations are conducted by a commercial unsteady RANS solver (Star CCM+) in head seas and the results are compared against HYDROS (LSST based), and the experimental results. Hebblewhite et al., (2007) conducted more than 500 experimental tests and obtained high-quality time history signals of the motions of the trimaran as well as the wave profiles, hence providing a valuable set of data for validation. Using the above-mentioned set of data, three different methods are compared, and the main differences are discussed.

The Turbulence models (SST Menter K-Omega and Realizable K-Epsilon) were studied and reliability analysis for gridding systems, boundary conditions and time discretization methods were performed. The time series of the heave and pitch motions were analysed in 18 cases and the transfer functions obtained for Froude numbers of 0.3 and 0.5 (equivalent speeds of 1.19 and 1.98m/sec at model scale) were analysed by three different methods. The sources of the discrepancy are analysed, and the physics of the phenomena are discussed.

Moreover, there is a discussion here as to whether CFD can be utilised as an alternative to expensive experimental tests in the future. The findings show that, as a result of considering green seas, hull shape above waterline and breaking waves, CFD methods are more efficient than LSST methods. Besides, due to the three-dimensional modelling, nonlinearity and viscosity effect, strip theory methods are less reliable than CFD methods.

The accuracy of the calculations need improvement for analysing frequencies at maximum motions response. As Kim et al., 2016 suggested, the discrepancy may be due to the wave deflection/diffraction phenomena in CFD, and/or wave resonance phenomenon in frequencies of maximum response (Field and Wayne, 2013, Jiang et al., 2018, Molin et al., 2009, Sun et al., 2010, Tan et al., 2017). The longer-term underlying purpose of the work presented in this paper is to develop the numerical CFD capability for predicting roll motions in oblique seas so as to better understand the geometric parameters influencing trimaran roll.

## **2. AMC TOWING TANK EXPERIMENTS AND HYDROS COMPUTATIONS**

Hebblewhite et al. (2007) studied the interaction effects of outriggers on the motions of a trimaran test model. Figure. 1 shows the trimaran model used in their study.

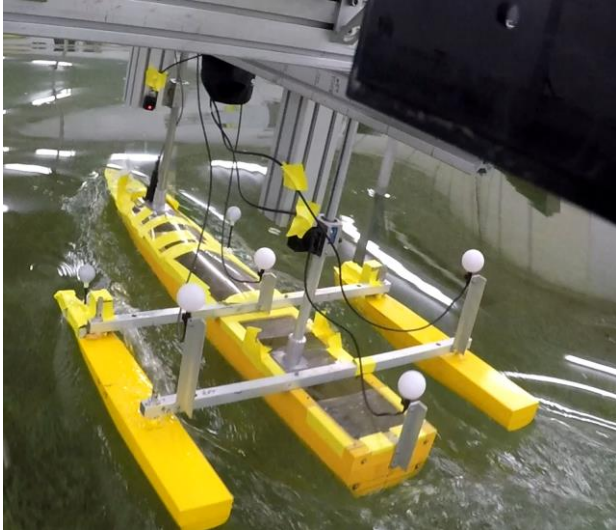


Figure 1. The trimaran Model tested at AMC towing tank (Hebblewhite et al., 2007).

A schematic diagram of the model is shown in Figure.2, and Table 1 summarises the main particulars. The testing hull form was based on Model 9 of the Australian Maritime Engineering CRC systematic series. More details were given by Hebblewhite et al., 2007.

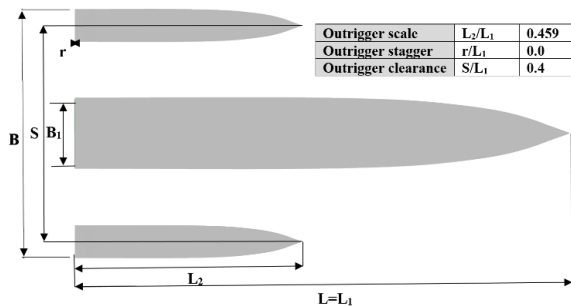


Figure 2. Geometric parameters of the 1.6 m trimaran model (Nowruzi et al., 2019).

Table 1. Details of the trimaran model 9 (Hebblewhite et al., 2007).

Item	Symbol	Value
Displacement mass (kg)	$\Delta$	12.8
Waterline length (m)	$L$	1.6
Waterline beam (m)	$B$	0.2
Draft (m)	$T$	0.08
Waterplane-area coefficient	$C_{WP}$	0.796
Maximum section coefficient	$C_M$	0.8
Block coefficient	$C_B$	0.5
Prismatic coefficient	$C_P$	0.624
Slenderness coefficient	$L/\nabla^{1/3}$	6.817
Outrigger displacement mass(kg)	$\Delta_s$	3.18
Outriggers scale ratio	$L_2/L$	0.459
Outriggers stagger ratio	$r_2/L$	0
Outriggers spacing (clearance ratio)	$Cl=s/L$	0.4
Pitch Radius of Gyration	$RoG$	0.4

The model tests undertaken by Hebblewhite et al. were carried out in the AMC towing tank with four Froude numbers ranging between 0.3 and 0.6. For further details refer to Hebblewhite et al. (2007).

HYDROS computations use a boundary element method for the computation of added mass and damping of ship's sections (Doctors, 1988). The ship motion prediction is based on the LSST method of Salvesen et al. (1970). Further detail of the numerical software developed by Doctors has been described by Doctors (1993).

### 3. TRIMARAN CFD NUMERICAL COMPUTATIONS IN HEAD SEAS

The numerical analysis undertaken in the research presented in this paper arises from using the software STAR CCM+ (CD-Adapco, 2017). The software solves Equation (1) for the translation of the centre of mass of a body in the global inertial coordinate system.

$$m \frac{dv}{dt} = f \quad (1)$$

Where  $m$  represents the mass of the body,  $f$  is the resultant force acting on the body and  $v$  is the velocity of the centre of mass. The equation of rotation of the body is also formulated in the Body Local Coordinate System with the origin at the centre of mass of the body (Equation 2):

$$M \frac{d\bar{\omega}}{dt} + \bar{\omega} \times M \bar{\omega} = n \quad (2)$$

Where  $M$  is the tensor of the moment of inertia,  $\bar{\omega}$  is the angular velocity of the rigid body and  $n$  is the resultant moment acting on the body. The tensor of the moments of inertia is expanded as shown by Equation 3.

$$M = \begin{pmatrix} M_{xx} & M_{xy} & M_{xz} \\ M_{xy} & M_{yy} & M_{yz} \\ M_{xz} & M_{yz} & M_{zz} \end{pmatrix} \quad (3)$$

To obtain the Reynolds-Averaged Navier-Stokes (RANS) equations, the Navier-Stokes equations for the instantaneous velocity and pressure fields are decomposed into a mean value and a fluctuating component. The averaging process may be thought of as time averaging for steady-state situations and ensemble averaging for repeatable transient situations. The resulting equations for the mean quantities are essentially equal to the original equations, except that an additional term known as the Reynolds stress tensor appears in the momentum transport equation given by Equation 4.

$$T_i \equiv -\rho \overline{v'v'} = -\rho \begin{pmatrix} \overline{u'u} & \overline{u'v'} & \overline{u'w'} \\ \overline{u'v'} & \overline{v'v'} & \overline{v'w'} \\ \overline{u'w'} & \overline{v'w'} & \overline{w'w'} \end{pmatrix} \quad (4)$$

To solve the defined problem, the Reynolds stress tensor  $T_i$  of the above equation in terms of the mean flow quantities should be modelled for the closure of the governing equations. Two basic approaches of Eddy viscosity models (K-Epsilon and K-Omega turbulence models) are employed. Eddy viscosity models use the concept of a turbulent viscosity  $\mu_t$  to model the Reynolds stress tensor as a function of mean flow quantities. These models solve additional transport equations for scalar quantities that enable the turbulent viscosity  $\mu_t$  to be derived. Reynolds stress transport models, known as second-moment closure models, solve transport equations for each component of the Reynolds stress tensor (CD-Adapco, 2017).

For realizable K-Epsilon and SST Menter K-Omega turbulence models, the turbulent viscosity is calculated through equations 5 and 6, respectively.

$$\mu_t = \rho C_\mu \frac{k^2}{\varepsilon} \quad (5)$$

$$\mu_t = \rho k T \quad (6)$$

Where  $\rho$  is density,  $k$  is turbulent kinetic energy,  $\varepsilon$  is turbulent dissipation rate,  $T$  is Viscous stress tensor and  $C_\mu$  is realizable time scale coefficient.  $T$  and  $C_\mu$  are not constant and are calculated independently.

In order to simulate realistic ship motions, a Dynamic Fluid Body Interaction (DFBI) model was used with the vessel free to move in the pitch and heave directions. The DFBI model enabled the RANS solver to calculate the exciting force and moments acting on the ship hull due to waves, and to solve the governing equations of rigid body motion in order to re-position the rigid body.

The Volume of Fluid (VoF) model was used to simulate flows of a pair of immiscible fluids (Air and Water) on numerical grids and to resolve the interface between the phases. In mathematical terms, Volume of Fluid model utilizes a Eulerian framework in its formulation. Setting up simulations for this approach involves use of distinct Eulerian phases. Thus, a common framework, the Eulerian Multiphase model, is used to create and manage two phases (i.e. air and water) and how they interact with each other.

The spatial distribution of each phase at a given time is defined in terms of a variable that is called the volume fraction. A method of calculating such distributions is to solve a transport equation for the phase volume fraction. For instance, a value of 0.5 for the volume fraction of water implies that a computational cell is filled with 50%

water and 50% air. This value therefore indicates the position of the water–air interface, which corresponds to the free surface.

In order to obtain sharp interfaces between the phases, the 2nd-order discretization scheme is used.

VOF waves are used to simulate the regular surface gravity waves on a light fluid (air) - heavy fluid (water) interface. They are used with the Volume of Fluid (VOF) multiphase model with the three degree of freedom motion model. When created, VOF waves provide field functions that can be used to initialize the VOF calculation and to provide suitable profiles at boundaries.

A first order wave is modelled with a first order approximation to the Stokes theory of waves. This approximation generates waves that have a regular periodic sinusoidal profile.

The 3D model was designed and imported as a Parasolid surface and the CFD domain was created based on the parameters as shown in Table 2. The dimensions of the domain fulfil ITTC Procedures (2011). The dimensions of the domain do not match those of the towing tank at AMC. However, they exceed the towing tank dimensions. In other words, boundaries reverse flow effects in the simulation is zero and the calculations are not affected by the boundary conditions.

Table 2. CFD domain dimensions, where  $L_{pp}$  is the length between perpendiculars of the main hull and  $B$  is the overall width of the model

Dimensions	AMC Towing tank (m)	Simulation domain (m)	ITTC recommendations
Width (m)	3.55	$5 > 2^* L_{pp} + B$	$2^* L_{pp} + B$ (~3 m)
Length (m)	100	11 ( $6^* L_{pp}$ )	$5-7 L_{pp}$
Depth (m)	1.5	1.7	$L_{pp}$ (1.7 m)

In the computational domain, an overset mesh was developed. to generate a high-quality grid configuration in the free surface region and in the proximity of the body (Field and Wayne, 2013). To reduce the calculation time, the overset region, which includes the trimaran hull body, moves with the hull (moving mesh) over a fixed background mesh of the domain. This saves computational time and allows the generation of a refined mesh system without compromising the accuracy. In order to improve the quality of the hull surface and optimize it for the volume mesh models, an automatic surface re-mesher tool is used to retriangulate the surface. The top, bottom, left and right boundaries of the domain can either be defined as wall boundary conditions (to model a virtual towing tank) or velocity inlet. Setting boundaries as a velocity inlet with a parallel

velocity component prevents the fluid interaction with boundaries and avoids development of a velocity gradient between the fluid and the wall (Date and Turnock, 1999). The velocity for the above-mentioned boundaries and the inlet boundary were set to the velocity of the trimaran tested in towing tank.

The final grid size in the free surface and around the hull is about 20 times smaller than the wave amplitude in accordance with ITTC recommendation (ITTC Procedures, 2011). The length to height ratio is less than 3, so the grids sizes in the longitudinal direction also meet the requirements. Figure.3 illustrates the details of mesh configuration as well as grid size in proximity of the free surface and far from the hull.

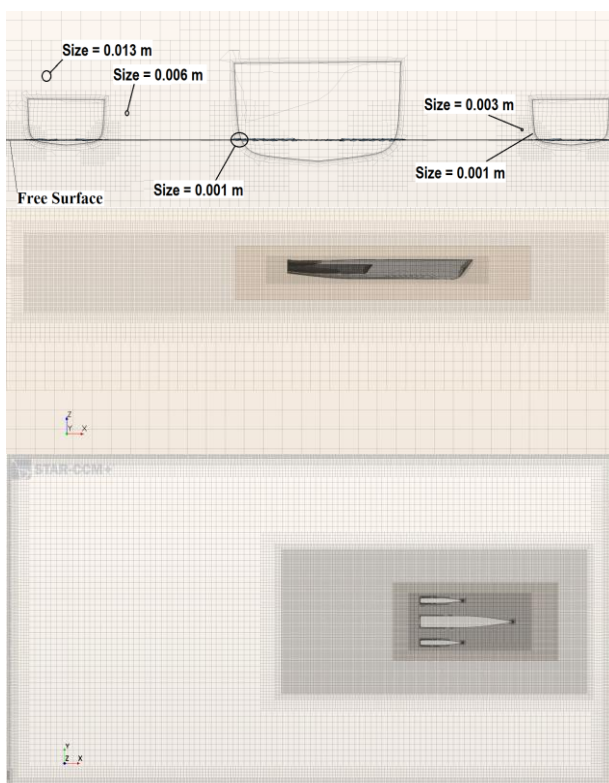


Figure 3. Front, side and top sectional view of the trimaran model in Star CCM+ showing mesh cell sizes including the free surface near and far from the hull.

### 3.1 RANS TURBULENCE MODELS' STUDIES

K-Epsilon and K-Omega models have shown their effectiveness in modelling ships in free surface, as there are large separations near the hull body (Arribas, 2007, Field and Wayne, 2013, Tezdogan et al., 2014b). K-Omega models are similar to K-Epsilon models in solving two transport equations, but they are different in the choice of the second transported turbulence variable.

The realizable K-Epsilon model contains a new transport equation for the turbulent dissipation rate ( $\epsilon$ ) (Shih et al.,

1995). Using two layers approach, the equation for the turbulent kinetic energy is solved in the entire flow (Rodi, 1991).

A K-Omega turbulence model is a two-equation model that solves transport equations for the turbulent kinetic energy,  $K$ , and the specific dissipation rate,  $\omega$ , that is, the dissipation rate per unit turbulent kinetic energy ( $\omega \approx \epsilon/k$ ), to determine the turbulent viscosity (Wilcox, 1993). (Menter, 1994) introduced a modification to the linear constitutive equation and dubbed the model containing this modification the SST (shear-stress transport) K-Omega model.

The two turbulence models mentioned above were utilised to examine their effectiveness in this study. In Figure.4, the motions are plotted against the physical time and the dimensionless wave frequency  $\omega_e^* = 5.75$ , this being the same as for the mesh studies.

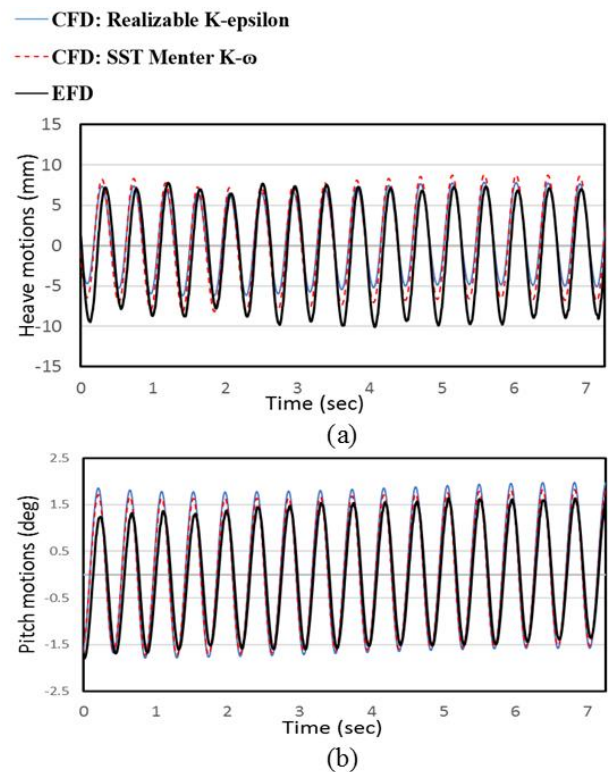


Figure 4. Results and verification of turbulence models' study for (a) heave motions and (b) pitch motions of the trimaran model in head waves. Froude number is 0.5 (forward velocity,  $V = 1.981$  m/s) and wave amplitude = 0.02 m. The time step size is 0.001 (sec) and the minimum cell dimensions near the water surface is 1.115 (mm).

Comparison with experiments, shown in Figure 4, proved the SST Menter K-Omega to be more accurate than realizable K-Epsilon. Therefore, the former, SST Menter K-Omega model, is used for the simulations.

### 3.2 CONVERGENCE AND RELIABILITY STUDY OF THE SIMULATIONS: MESH AND TIME STEP UNCERTAINTY

Before conducting the numerical simulations, it is necessary to specify the uncertainty in simulation results to ensure the numerical approach accurately simulates the physics. According to the verification method suggested by Stern et al. (2001), numerical uncertainty ( $U_{SN}$ ) consists of iterative convergence uncertainty ( $U_I$ ), grid-spacing uncertainty ( $U_G$ ) and time-step uncertainty ( $U_T$ ) and is given in Equation 7.

$$U_{SN}^2 = U_I^2 + U_G^2 + U_T^2 \quad (7)$$

The uncertainty of  $U_I$  is negligible (Enshaei, 2018). However, the grid spacing and time step as major sources of uncertainty were investigated here for heave and pitch transfer functions. Finally, the results of the fine mesh configuration with an efficient time step were compared against experimental data.

Three different mesh configurations (Table 3) with a refinement ratio of  $r_G = \sqrt{2}$  were considered for the model as shown in Table 4. The grid uncertainty was obtained with the smallest time step, which was 0.001 (sec). With the same approach, the time step uncertainty was investigated for the finest mesh configuration. The grid-spacing and time step uncertainty calculations were performed based on the Richardson extrapolation (Jin et al., 2016). Using this method, the error is expanded in a power series with integer powers of time step or grid spacing as a finite sum. However, just the first term of the series is considered as the solution is assumed to be in the asymptotic range.

The numerical model is virtually towed with a forward speed of 1.981 m/s and the wave frequency used was 1 Hz at a wave height of 40mm. The simulation results for the various cases of mesh refinement including coarse ( $S_3$ ), medium ( $S_2$ ) and fine ( $S_1$ ) are calculated by Equations 8-10, as given in Table 3.

$$\varepsilon_{G32} = S_3 - S_2 \quad (8)$$

$$\varepsilon_{G21} = S_2 - S_1 \quad (9)$$

$$R_G = \frac{\varepsilon_{G21}}{\varepsilon_{G32}} \quad (10)$$

Table 3. The number of mesh elements in different grid configurations

Mesh Refinement	Background cells	Overset cells	Total cells
Fine (1)	3,950,043	5,538,206	9,488,249
Medium (2)	1,862,000	2,869,103	4,731,103
Coarse (3)	867,207	1,700,488	2,567,695

where  $\varepsilon_{G32}$  is the variation of the simulation results for coarse and medium mesh configurations and  $\varepsilon_{G21}$  is the

variation of the simulation results for medium and fine mesh configurations.  $R_G$  is the convergence ratio. Four typical conditions can be defined for the convergence ratio,  $R_G$ :

- (i) Monotonic convergence ( $0 < R_G < 1$ ),
- (ii) Oscillatory convergence ( $R_G < 0$ ;  $|R_G| < 1$ ),
- (iii) Monotonic divergence ( $R_G > 1$ ), and
- (iv) Oscillatory divergence ( $R_G < 0$ ;  $|R_G| > 1$ ).

For the cases (iii) and (iv) the numerical uncertainty cannot be computed (Stern et al., 2006). For the case (ii) uncertainty can be computed based on bounding error between upper limit  $S_U$  and lower limit  $S_L$  using Equation 11 as follows:

$$U_G = \frac{1}{2} (S_U - S_L) \quad (11)$$

where  $U_G$  is the grid spacing uncertainty. The generalised Richardson extrapolation is adopted to compute the numerical error  $\delta_{RE_{G1}}^*$ , and the order of accuracy  $P_G$ , is obtained by Equations 12 and 13:

$$\delta_{RE_{G1}}^* = \frac{\varepsilon_{G21}}{r_G^{P_G} - 1} \quad (12)$$

$$P_G = \frac{\ln(\varepsilon_{G32} / \varepsilon_{G21})}{\ln(r_G)} \quad (13)$$

The correction factor  $C_G$ , which is defined by the Equation 14, determines the method of uncertainty calculation:

$$C_G = \frac{r_G^{P_G} - 1}{r_G^{P_{Gest}} - 1} \quad (14)$$

If  $C_G$  is close to 1, then the solutions are close to the asymptotic range. The numerical error  $\delta_{SN}^*$ , the benchmark result  $S_C$  and uncertainty  $U_{GC}$  can be computed from the following set of equations (Equations 15-17):

$$\delta_{SN}^* = C_G \times \delta_{RE_{G1}}^* \quad (15)$$

$$S_C = S - \delta_{SN}^* \quad (16)$$

$$U_G = \begin{cases} (9.6(1-C_G)^2 + 1.1) |\delta_{RE_{G1}}^*| & |1-C_G| < 0.125 \\ (2|1-C_G| + 1) |\delta_{RE_{G1}}^*| & |1-C_G| \geq 0.125 \end{cases} \quad (17)$$

If the value of  $C_G$  is much greater than 1, then the solutions are away from the asymptotic range and the numerical uncertainty ( $U_G$ ) can be determined as follows:

$$U_G = \begin{cases} (9.6(1-C_G)^2 + 1.1) |\delta_{RE_{G1}}^*| & |1-C_G| < 0.125 \\ (2|1-C_G| + 1) |\delta_{RE_{G1}}^*| & |1-C_G| \geq 0.125 \end{cases} \quad (18)$$

$\Delta t = 0.001$  was used according to ITTC recommendations for solving RANS equations. The time step uncertainty can be computed based on a similar procedure, starting from  $\Delta t = T/2^9$  (Kianejad et al., 2019) and considering a uniform refinement ratio of 2 ( $r_T=2$ ).

Considering that the cell sizes near the hull and boundaries were about 0.002, the Courant number is less than 1. The results of numerical simulations and the magnitude of uncertainties for each mesh configuration are presented in Table 4 & 5. It is apparent that the uncertainty of grid spacing is more than the uncertainty of the time step, accounting for about 6.25% and 2.71%, respectively. The magnitude of uncertainty for the pitch transfer function is higher than that for the heave transfer function. According to the results, the fine mesh configuration can simulate the motion characteristics relatively accurately. Further simulations were performed based on the fine mesh configuration and smallest time step.

Table 4. Grid convergence study, where  $r_G$  is grid spacing refinement ratio, and  $S_1$ ,  $S_2$  and  $S_3$  are variation of simulation results for fine, medium and coarse meshes, respectively.  $TF_3$  and  $TF_5$  are transfer functions for heave and pitch motions respectively.  $R_G$  is the convergence ratio,  $U_G$  is the grid uncertainty,  $\delta^*_{REGI} (\%S_i)$  is numerical error and  $R_G$  is the uncertainty of grid spacing.

Amplitude	$r_G$	$S_1$	$S_2$	$S_3$	$R_G$	$\delta^*_{REGI} (\%S_i)$	$U_G (\%S_i)$
$TF_3$	$\sqrt{2}$	0.39	0.32	0.20	0.58	2.51	3.58
$TF_5$	$\sqrt{2}$	0.33	0.37	0.49	0.38	3.12	6.25

Table 5. Time step convergence study, where  $r_T$  is time step refinement ratio, and  $T_1$ ,  $T_2$  and  $T_3$  are variation of simulation results for three time-steps.  $TF_3$  and  $TF_5$  are transfer functions for heave and pitch motions respectively.  $R_T$  is the convergence ratio,  $U_T$  is the grid uncertainty,  $\delta^*_{RETI} (\%T_i)$  is numerical error for time step and  $R_T$  is the uncertainty of time step.

Amplitude	$r_G$	$T_1$	$T_2$	$T_3$	$R_T$	$\delta^*_{RETI} (\%T_i)$	$U_T (\%T_i)$
$TF_3$	2	0.39	0.35	0.28	0.57	1.36	2.27
$TF_5$	2	0.33	0.35	0.40	0.45	1.52	2.71

For different wave frequencies, the simulation results for different grid and time step quality does not change significantly.

With a different wave height, however, the simulation results become more dependent on the grid and time step quality. This causes variation in all the parameters including numerical convergence ratio, oscillatory ratio and numerical uncertainty. The new uncertainty should be in a reasonable range. Otherwise, the cell sizes and time step value should be reset to improve the uncertainty percentage.

In this particular case, the simulations are conducted in a single wave height and the model can be used for higher waves. However, for lower waves, another uncertainty analysis in different cell sizes will be necessary.

#### 4. COMPARISON OF TRIMARAN EXPERIMENTAL DATA WITH NUMERICAL COMPUTATIONS

The results of the finest grid system and with the smallest time step at a defined condition were compared against experimental data from Hebblewhite et al. (2007). A numerical wave probe was put at a one-meter diagonal distance from the hull, so the wave amplitude and frequency were recorded closer to the hull to make sure that the physical and numerical conditions are the same. The heave and pitch motions are presented in Figure 5.

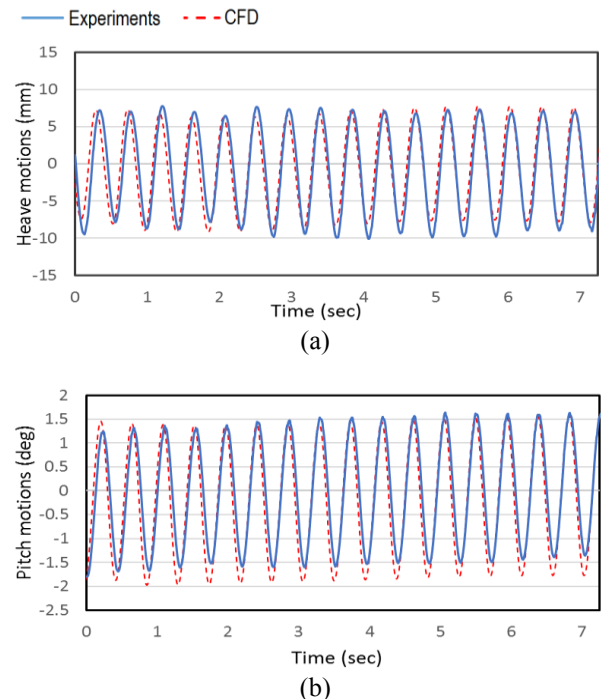


Figure 5. Mesh studies: Time histories of (a) heave and (b) pitch motions for the 1.6 m trimaran model in head waves at Froude number = 0.5 (velocity  $V=1.98$  m/s), wave amplitude = 0.02 m and dimensionless wave frequency = 5.75.

The longitudinal position of the outriggers (stagger ratio) in all simulations performed was considered zero ( $St=0.0$ ). Therefore, the transoms of the outriggers remain in line with the transom of the main hull. The clearance ratio was set to be constant at  $Cl = 0.4$ . This set-up was chosen primarily due to the availability of the experimental data undertaken by Hebblewhite et al. (2007). The wave amplitude was made constant and set to 20 mm. The effect of speed on the motions is studied by a comparative study using CFD methods, HYDROS and experimental test results. The speed was set to 1.189 m/s and 1.981 m/s.

The simulation results for the vessel moving with a speed of 1.981m/s in head waves with dimensionless wave encounter frequency of 5.75 and wave height of 40 mm are presented in Figure.6. The wave height and frequency are set the same as were measured in the experiments (Figure.6a). The wave interaction of the three hulls of the vessel are evident in Figure.6b.

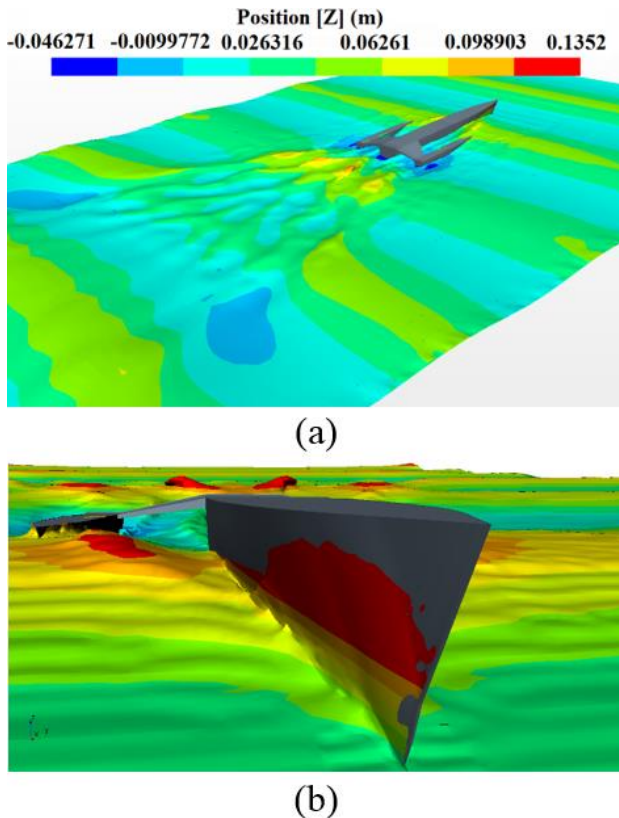


Figure 6. CFD simulation of the trimaran moving with the speed of 1.981 in head waves with dimensionless encounter frequency of 5.75 and height of 40 mm. (a) Generated wave in the domain (b) the wave interaction between the main hull and the outriggers.

#### 4.1 TIME HISTORY OF HEAVE AND PITCH MOTIONS

This section presents two sets of time histories for verification of computational results against experimental data collected at two different speeds. The results are shown in Figures 7 and 8 at a model test speed of 1.189 m/s (Froude Number = 0.3) and 1.981 m/s (Froude Number = 0.5) respectively. The stagger and clearance ratios for all cases remained constant, at 0.0 and 0.4 respectively. The heading

angle was set at 180 degrees to represent a simulation in heads seas similar to the model tests undertaken by Hebblewhite et al. (2007). The time series results shown are plotted for dimensionless wave encounter frequencies of 1.5, 3.3 and 5.75 in Figure.7 (Froude Number = 0.3), and 1.5, 4.7 and 7.7 in Figure.8 (Froude Number = 0.5). The numerical results predicted match the experimental data reasonably well in particular for the frequency of the largest motions response. In some cases, the CFD either over predicts or under predicts the heave or pitch amplitude but overall there is good correlation at these specific frequencies as shown in the following figures.

In Figure.7, at  $\omega_e^* = 1.51$ , it can be seen that the CFD predicts the heave amplitude reasonably well. It is evident that there is an initial shifting of the phase in the CFD results shown in Figure.7 before the CFD becomes cyclically regular at the same frequency as the experimental data. This is caused by the decay of the initial transient in the CFD, with the experimental data being in regular motion at the start time of Figure.7. At  $\omega_e^* = 4.88$  we see that the CFD underestimates the peaks when compared to the experiment but there is not a significant shift of the heave phase as the initial condition of the CFD is better matched to the regular heave motion of the ultimately regular heave motion in this case. At  $\omega_e^* = 7.67$  we see that the initial CFD condition is again well matched to the regular motion of the experiments.

For pitch motions, at  $\omega_e^* = 1.51$ , the CFD predicts the amplitude reasonably well but there is an initial shifting of the phase over the first few cycles, similar to that explained above for the heave motion. At  $\omega_e^* = 4.88$ , the CFD underestimates also the peak pitch when compared to experiment but there is a negligible shifting of the phase due to decay of the initial transient since the initial condition is better matched to the ultimate regular pitch motion as was also the case for heave at this frequency. At  $\omega_e^* = 7.67$  there is again very little shifting of the phase since the initial condition is again well matched to the ultimate regular motion and the CFD follows the experimental results closely in time.

As shown in Figure.8, for the higher speed, at  $\omega_e^* = 1.51$ , the CFD predicts the heave amplitude reasonably well whilst for the pitch motion, the CFD underestimates the peak values. At  $\omega_e^* = 4.88$ , for both heave and pitch motions there is consistency between the phase of experimental data and CFD results as the initial condition of the CFD was closely matched to the ultimate regular motion as explained above at the lower speed. At  $\omega_e^* = 7.67$  the phase is again well matched at the initial condition and the CFD follows the experimental results closely in both heave and pitch. However, the CFD underestimates the peaks in the pitch motions when compared to experiment but there is good prediction of the heave motion amplitudes.

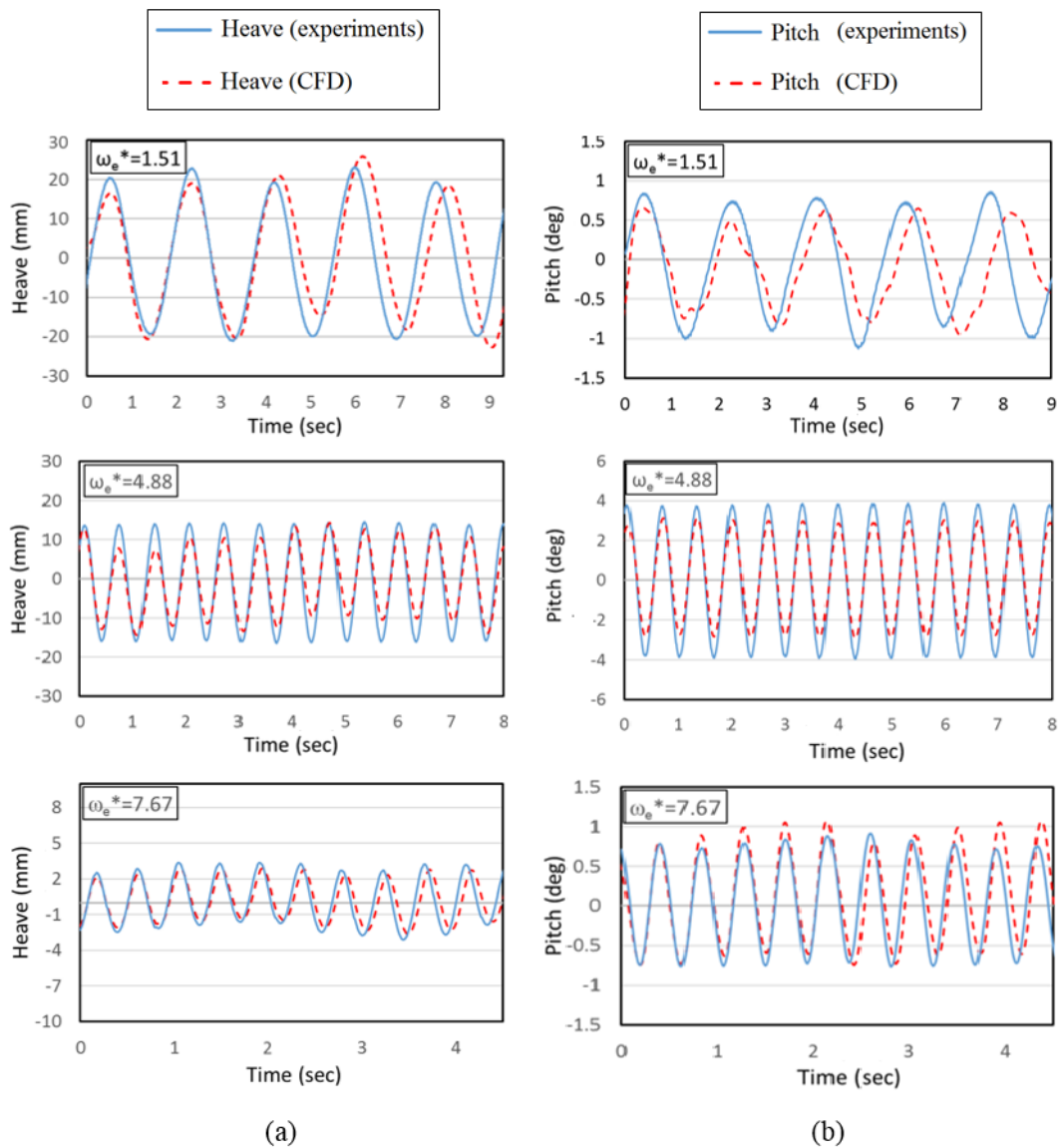


Figure 7. Comparison of Trimaran experimental model test results with CFD: (a) heave and (b) pitch motions at dimensionless wave encounter frequencies of  $\omega_e^* = 1.51, 4.88$  and  $7.67$  at a wave amplitude of  $0.02\text{m}$  and Froude number  $0.3$ .

Figure 8. Comparison of Trimaran experimental model test results with CFD: (a) heave and (b) pitch motions at dimensionless wave encounter frequencies of  $\omega_e^* = 1.51, 3.34$  and  $5.75$  at a wave amplitude of  $0.02\text{m}$  and Froude number  $0.5$ .

We have seen that in some cases, there is a phase shift between the measured experimental data and CFD time histories, which is a result of the decay of the initial CFD transient and associated shifting of the phase in the computations. The other possible cause of discrepancies between experimental and CFD results is the mechanism of wave-wind interaction, wave-boundaries interaction and wave-current interaction (Banks and Abdussamie, 2017) not included in the CFD here. Since mesh and turbulence models have been investigated in detail as described earlier and the initial conditions are set similar to the experimental test conditions, these discrepancies appear to be related to the limitations of the numerical capability.

CFD models a moving hull in head waves by simulating a situation where the hull remains steady (zero speed) and the current and wind move towards the ship thus simulating the ship's forward speed. This is well known as the difference between Lagrangian and Eulerian approaches (Nakayama, 2018).

This difference causes wave deformation. The deformation is a consequence of the interactions between wave, current and wind (Kim et al., 2016). Wind speed causes the waves to break at an earlier stage than in no-wind conditions. A current in the same direction with wave stretches the wavelength, while a current with an opposing direction shortens it, similar to the Doppler shift effect in waves due to steady current (API, 2000). The significance of this phenomenon appears to be greater at higher speeds and in frequencies with maximum response.

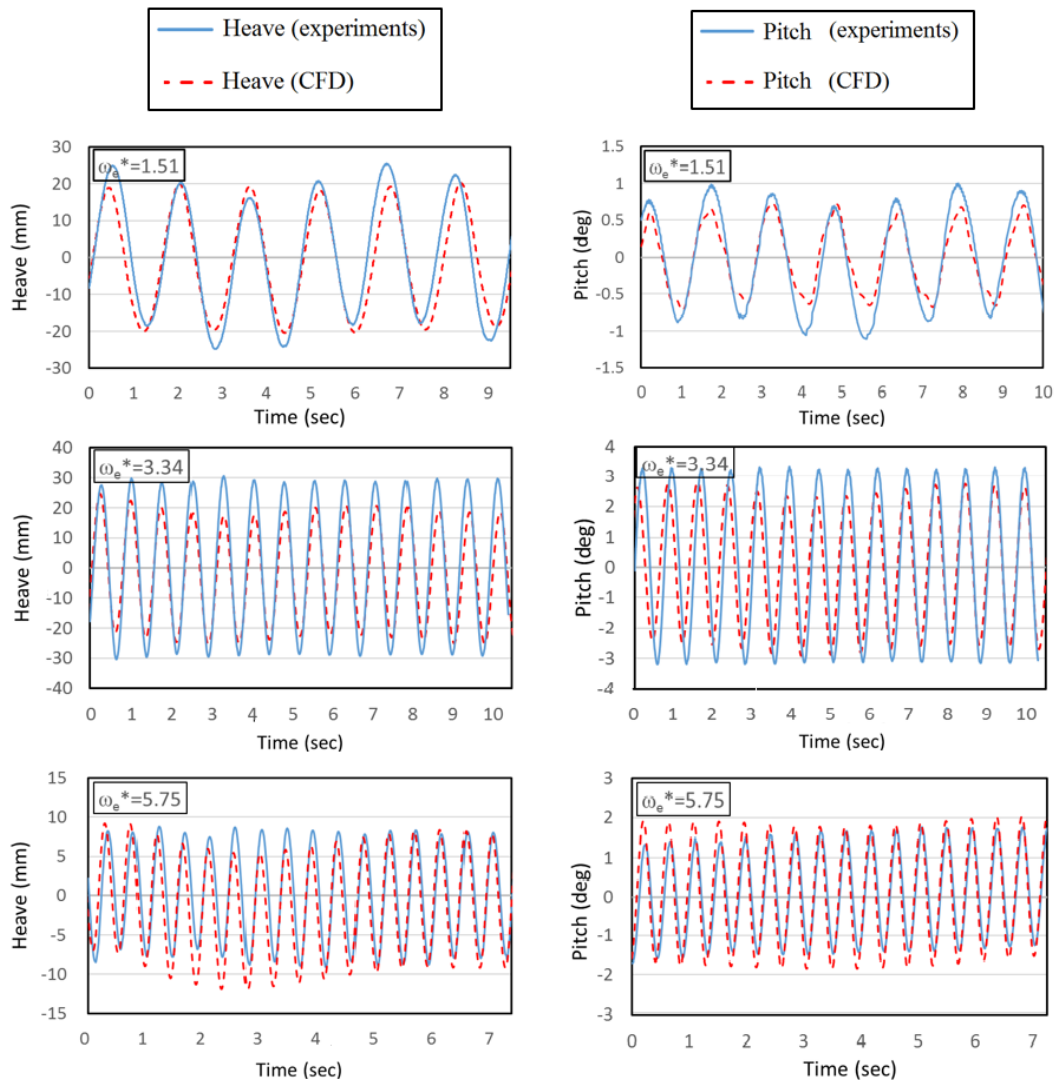


Figure 8. Comparison of Trimaran experimental model test results with CFD: (a) heave and (b) pitch motions at dimensionless wave encounter frequencies of  $\omega_e^* = 1.51, 3.34$  and  $5.75$  at a wave amplitude of  $0.02\text{m}$  and Froude number  $0.5$ .

#### 4.2 RESPONSE AMPLITUDE OPERATORS OF TRIMARAN MOTIONS IN HEAD SEAS

The Response Amplitude Operators of the  $1.6\text{ m}$  trimaran model were determined based on the numerical results obtained using linear LSST (Hebblewhite, Sahoo and Doctors 2007), CFD (computed as presented in this paper) and the experimental model test results of Hebblewhite, Sahoo and Doctors (2007). All the results pertain to the seakeeping behaviour of the specific trimaran tested in this study.

Figure.9 shows the heave and pitch Response Amplitude Operators (RAOs) obtained for speeds of  $1.189\text{ m/s}$  and  $1.981\text{ m/s}$  at a set wave height of  $40\text{ mm}$ . The linear LSST is one of the earliest developments in this field of study to investigate the effect of head sea theoretically (Doctors, 2015). Doctors obtained promising results in predicting the motions of a multihull, although he assumed the geometry of the

model is irrelevant above the calm waterline. The response amplitudes for the trimaran in  $20\text{mm}$  waves are plotted against dimensionless wave encounter frequency, in Figures 9a and 9b for the low speed case ( $1.189\text{ m/s}$ ) and Figures 9c and 9d for the high-speed case ( $1.981\text{ m/s}$ ). The trend of numerical plots computed by HYDROS (Hebblewhite et al., 2007) for the heave motions as shown in Figure.9c appear to be consistent with the experimental results. However, the assumption of linearity, which neglects the effect of variations in the hull planform above and below the waterline, makes the pitch motion results less consistent with the experiments. Moreover, it does not capture the maximum of the pitch RAO at the frequency of maximum normalised response. On the other hand, the CFD results are in better agreement with the experiments for both heave and pitch motion normalised amplitudes with trends similar to the towing tank tests at both Froude numbers.

In Figure.9a, it is evident that the magnitude of the transfer function for heave starts at 1 at low frequency and reduces to small values at high wave encounter frequency as expected. More importantly, there is a resonant response at  $\omega_e^*$  of 5.7. The LSST method predicts the resonance response at  $\omega_e^* = 4.0$ , and the motions taper off much earlier at  $\omega_e^* = 6.2$ . In comparison, the CFD computations compare relatively well with the experimental results whilst also predicting more accurately the resonant peak at  $\omega_e^* = 5.7$ .

In Figure.9b, the pitch transfer function starts at 1 at low frequency and approaches zero at high wave encounter frequencies. The resonant response occurs at  $\omega_e^*$  of 4. Following this there is a rapid reduction of the response in pitch at frequencies above the resonant peak. The CFD prediction correlates well with the experimental data in some wave frequencies but it underestimates the pitch motions at the frequencies of  $\omega_e^* = 3\sim 5$ . As mentioned in the previous section, this may be due to the wave deformation. The LSST results taper off more rapidly with frequency and do not capture the resonant peak well.

In Figure.9c, the magnitude of the transfer function for heave starts at 1 at low frequency and then approach small values at high encounter wave frequency. The maximum heave response of 1.4 is identified at an encounter frequency of  $\omega_e^* = 4.1$  after which a rapid reduction occurs at higher frequency. Both LSST and CFD motion predictions for heave correlate very well with the experimental data at Froude number of 0.5 over the entire range of wave encounter frequencies tested. In this case the LSST more closely matches the experimental results whilst the CFD is observed to slightly under predict the resonant response.

In Figure.9d, the experimental results show a peak magnitude of the transfer function for pitch at 1.3 and it occurs at a dimensionless wave encounter frequency of  $\omega_e^* = 3.4$ . In this case both the CFD and LSST results correlate well with the experiments at the higher frequencies but the CFD results underestimate the pitch motions at lower and resonant wave encounter frequencies. The LSST method, however, shows the response tapering off without a resonant peak.

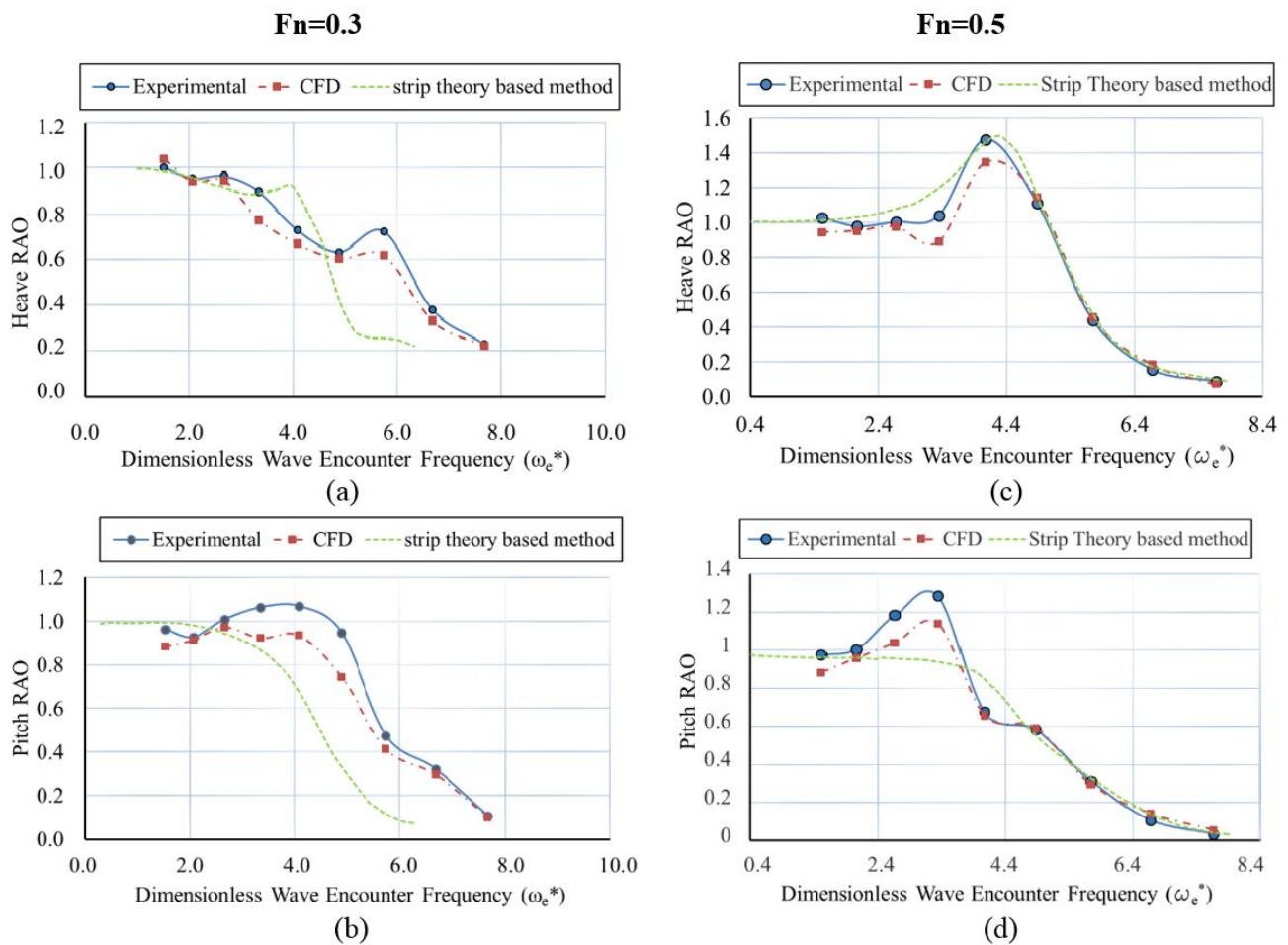


Figure 9. Heave and Pitch response of the trimaran model in head seas at Froude number =0.3 and 0.5 (model test speed of 1.189 and 1.981 m/s respectively) and wave amplitude = 20 mm: CFD calculation (computed in this study), Strip Theory (Hydros) and experimental data from (Hebblewhite et al., 2007).

It is apparent from the above figures that a CFD method is more reliable in predicting the trimaran motions in head seas when compared to LSST.

## 5. DATA ANALYSIS AND SOURCES OF DISCREPANCY

The potential mechanisms behind the discrepancy between the experimental results and the LSST methods has been discussed earlier by Hebblewhite et al. (2007). Therefore, this section further discusses the factors that may introduce errors in the CFD calculations or in towing tank tests. Observations made during the tests in head seas show that there has been a wide range of conditions where there would be green water on the deck during these tests, plastic protective sheets being used to avoid encountered green water over the bow in some cases. Green water is one of the potential errors expected in conducting simulations in CFD (Figure.6a).

Another source of discrepancy is reported by Sun et al. (2010), where the wave resonance (wave deflection/diffraction) occurs. That is in a case when two fixed structures are within the close proximity of each other (i.e. main hull and outriggers). Measurements of wave resonance for trimaran hull shapes is challenging both experimentally and numerically and depends heavily on the spacing between the different hulls and the wave elevation, the waterline at each hull being fixed and the ratio of the width of the hull to the width of the hull spacing (Jiang et al., 2018). Molin et al. (2009) suggested that the difference between numerical data and experimental results is due to the flow separation at the bilge. In his comparative study, the numerical analysis and experimental data have discrepancies in all conditions. Sen (2016) also investigated the effect of damping effects in using numerical CFD viscous methods by simulating the multi hull bodies in free surface. He suggested that the nonlinearity of the damping could be the source of discrepancy.

As discussed by other researchers, one potential mechanism behind the discrepancies is the occurrence of wave resonance. Therefore, the effect of wave deflection between two/three non-barge bodies on the motions of a multihull ship should be further investigated. As seen above, Figure.6b shows the occurrence of wave deflection between the three hulls in CFD, an effect not represented in the LSST.

Overall, even with some discrepancies, the CFD method demonstrates a significant improvement when compared to strip theory-based methods in predicting the motions of trimarans at high speeds.

## 6. CONCLUSIONS

The results of the numerical CFD method using RANS equations has demonstrated good correlation with the experimental data for determining the response of a 1.6m trimaran model in head seas. This is evident when comparing the CFD results to those measured

experimentally as shown by the RAOs for both heave and pitch motions, although there are slight variations at some frequencies.

The CFD simulation time records have a good resemblance to the towing tank data at most frequencies. However, in some cases, the calculated motion response is slightly higher than the measured experimental value. This seems to mostly happen at the frequencies of maximum response. A possible source of discrepancy may be considered wave deformation at each wave frequency. This deformation is a consequence of the interactions between wave, current and wind. The significance of this phenomenon is greater at higher speeds ( $F_n > 0.5$ ) and lower frequencies ( $\omega^* < 4.4$ ).

Wave resonance phenomenon occurs between the outriggers and the main hull of the trimaran, which makes the motion prediction more challenging. This resonance depends on several parameters such as hulls spacing, ratio of the width of the hull to the width of the hull spacing, wave elevation and waterline length as well as relative speed of each hull.

Based on the results from HYDROS it has been shown that the assumption of linearity causes the pitch motion data predicted to be less consistent with the experimental test results. Assuming the experimental results were accurate with minimal sources of error in the measured data, the CFD results have been shown to produce a mean error of less than 10%. The strip theory-based methods are, however, unreliable in terms of predicting the motions in some cases. This may be due to nonlinearity and Viscous effects.

Overall the CFD method applied here has improved the predicted motions response for a trimaran in head seas when compared to HYDROS strip theory results. Based on the developing confidence in the techniques adopted here it is now proposed to extend computation to oblique seas where trimaran roll is of particular importance.

## 7. ACKNOWLEDGEMENTS

This research was undertaken with the support of the University of Tasmania and the Australian Maritime College. The authors take this opportunity to express their profound gratitude to the staff of the Australian Maritime College Ship Hydrodynamic Centre for providing previous experimental data. Access to the work of Hebblewhite et al. (2007) at the Australian Maritime College is also gratefully acknowledged.

## 8. REFERENCES

1. API 2000. *Recommended practice for planning, designing and constructing fixed offshore platforms*. working stress design.
2. ARMSTRONG, T. & HOLDEN, K. 2003. *A new generation of large fast ferry-from concept*

- to contract reality. FAST 2003, 75-84. Ischia, Italia.
3. ARRIBAS, F. P. 2007. *Some methods to obtain the added resistance of a ship advancing in waves.* Ocean Engineering, 34, 946-955.
  4. BANKS, M. & ABDUSSAMIE, N. 2017. *The response of a semisubmersible model under focused wave groups: Experimental investigation.* Journal of Ocean Engineering and Science, 2, 161-171.
  5. BECK, R., REED, A., SCLAVOUNOS, P. & HUTCHISON, B. 2001. *Modern computational methods for ships in a seaway.* Discussion. Author's closure. Transactions-Society of Naval Architects and Marine Engineers, 109, 1-51.
  6. BOOTE, D., COLAIANNI, T. & PINO, E. *Seakeeping analysis of a trimaran fast ferry.* 4th International Conference of High-Performance Marine Vehicle (HIPER), 304-316., 2004. 304-316.
  7. CD-ADAPCO 2017. *User guide, STAR-CCM+.* Star-CCM+.
  8. DATE, J. C. & TURNOCK, S. R. 1999. *A Study into the Techniques Needed to Accurately Predict Skin Friction Using RANS Solvers with Validation Against Froude's Historical Flat Plate Experimental Data.* Ship Science Report. Southampton, UK: University of Southampton,.
  9. DOBASHI, J. 2014. *On the prediction method for ship motions of trimaran in oblique waves.* Journal of the Japan Society of Naval Architects and Ocean Engineers, 20, 77-84.
  10. DOCTORS, L. *Application of the boundary-element method to bodies oscillating near a free surface.* International Symposium on Computational Fluid Dynamics ISCFD, 1:377-386, August 24-27 1988 Sydney, Australia. 377-386.
  11. DOCTORS, L. 1993. *HYDROS: integrated software for the analysis of the hydrostatics and hydrodynamics of marine vehicles.* 10th international Maritime and Shipping Symposium (ShipShape 2000), 1:373-392. The University of New South Wales, Australia.
  12. DOCTORS, L. & SCRACE, R. *The optimization of trimaran sidehull position for minimum resistance.* Seventh International Conference on Fast Transportation (FAST 2003), October 2003 2003 Ischia, Italy. 1-12.
  13. DOCTORS, L. J. 2015. *Hydrodynamics of high-performance marine vessels,* CreateSpace Independent Publishing Platform, 2:247.
  14. DU, L., HEFAZI, H. & SAHOO, P. 2019. *Rapid resistance estimation method of non-Wigley trimarans.* Ships and Offshore Structures, 1-11.
  15. FACH, K. 2004. *Classification aspects of HSC multihulls.* 4th International Conference on High-Performance Marine Vehicle (HIPER), 317-322.
  16. FALTINSEN, O., LANDRINI, M. & LUGNI, C. *Hydrodynamic Aspects of High-Speed Vessels.* Proc. 7th International Conference on Fast Sea Transportation, 1:13-22, 2003. 13-22.
  17. FALTINSEN, O. & ZHAO, R. 1991. *Numerical predictions of ship motions at high forward speed.* Phil. Trans. R. Soc. Lond. A, 334, 241-252.
  18. FANG, M. C. & TOO, G. Y. 2006. *The effect of side hull arrangements on the motions of the trimaran ship in waves.* Naval engineers journal, 118, 27-37.
  19. FIELD, P. L. & WAYNE, L. N. *Comparison of RANS and Potential Flow Force Computations for the ONR umble home Hull form in Vertical Plane Radiation and Diffraction Problems.* ASME 2013 32nd International Conference on Ocean, Offshore and Arctic Engineering, June 9-14, 2013 2013. Virginia Polytechnic Institute and State University, Blacksburg, VA., 23.
  20. GHADIMI, P., NAZEMIAN, A. & GHADIMI, A. 2019. *Numerical scrutiny of the influence of side hulls arrangement on the motion of a Trimaran vessel in regular waves through CFD analysis.* Journal of the Brazilian Society of Mechanical Sciences and Engineering, 41, 1.
  21. GRAFTON, T. J. 2007. *The roll motion of trimaran ships.* Doctor of Philosophy, University College London.
  22. ENSHAEI, H., KIANEJAD, S. 2018. *Quantifying Ship's Dynamic Stability through Numerical Investigation of Weight Distribution.* Proceedings of the 13th Int. Conference on the Stability of Ships and Ocean Vehicles (STAB), Kobe, Japan.
  23. HEBBLEWHITE, K., SAHOO, P. K. & DOCTORS, L. 2007. *A case study: theoretical and experimental analysis of motion characteristics of a trimaran hull form.* Ships and Offshore Structures, 2, 149-156.
  24. ITTC PROCEDURES 2011. *Guidelines.* 2011. *Practical Guidelines for Ship CFD Applications.* ITTC.
  25. JERSEY ACTION GROUP 2016. *Temporary Ferry Tenerife is shaken violently by the waves in Los Cristianos.* <https://www.youtube.com/watch?v=Yi4iU0a56-M>. Jersey Action Group (accessed 07<sup>th</sup> July 2017)
  26. JIANG, S. C., BAI, W. & TANG, G. Q. 2018. *Numerical simulation of wave resonance in the narrow gap between two non-identical boxes.* Ocean Engineering, 156, 38-60.
  27. JIN, Y., CHAI, S., DUFFY, J., CHIN, C., BOSE, N. & TEMPLETON, C. 2016. *RANS prediction of FLNG-LNG hydrodynamic interactions in steady current.* Applied Ocean Research, 60, 141-154.
  28. JT901 2015. *Condor Liberation rough crossing Poole to Jersey high seas.* In: YOUTUBE (ed.)

- <https://www.youtube.com/watch?v=Gf3QwpOkovs>. (Accessed 07<sup>th</sup> July 2017)
29. KIANEJAD, S., ENSHAEI, H., DUFFY, J. & ANSARIFARD, N. 2019. *Prediction of a ship roll added mass moment of inertia using numerical simulation*. Ocean Engineering, 173, 77-89.
  30. KIM, M.-G., JUNG, K.-H., PARK, S.-B., LEE, G.-N., PARK, I.-R. & SUH, S.-B. 2019. *Study on Roll Motion Characteristics of a Rectangular Floating Structure in Regular Waves*. Journal of Ocean Engineering and Technology, 33, 131-138.
  31. KIM, S.-Y., KIM, K.-M., PARK, J.-C., JEON, G.-M. & CHUN, H.-H. 2016. *Numerical simulation of wave and current interaction with a fixed offshore substructure*. International Journal of naval Architecture and ocean engineering, 8, 188-197.
  32. LINDSTROM, J., SIRVIO, J. & YLI-RANTALA, A. *Superslender monohull with outriggers*, 1:295. 1995 Lubek Travemunde, Germany. 295.
  33. MENTER, F. R. 1994. *Two-equation eddy-viscosity turbulence models for engineering applications*. AIAA journal, 32, 1598-1605.
  34. MOLIN, B., REMY, F., CAMHI, A. & LEDOUX, A. *Experimental and numerical study of the gap resonances in-between two rectangular barges*. 13th congress of international maritime association of mediterranean, 2009.
  35. NAKAYAMA, Y. 2018. *Introduction to fluid mechanics*, Butterworth-Heinemann.
  36. NEWMAN, J. N. 1979. *The theory of ship motions*. Advances in applied mechanics. Elsevier.
  37. NOWRUZI, H., ENSHAEI, H., LAVROFF, J., KIANEJAD, S. S. & DAVIS, M. R. 2019. *Motions and added resistance of a high-speed trimaran in regular oblique waves*. International Conference on Ships and Offshore Structures, ICSOS 2019. Florida, USA.
  38. ONAS, A. S. 2009. *Nonlinear roll motions of a frigate-type trimaran and susceptibility to parametric roll resonance*. Doctor of Philosophy, Stevens Institute of Technology.
  39. PATTISON D, ZHANG J. *Trimaran ships*. Proceedings of the RINA Spring Meetings Paper; 1994.
  40. RODI, W. *Experience with two-layer models combining the k-epsilon model with a one-equation model near the wall*. 29th Aerospace sciences meeting, 1991. 216.
  41. SALVESEN, N., TUCK, E. & FALTINSEN, O. 1970. *Ship motions and sea loads*. Trans. SNAME, 78, 250-287.
  42. SEN, D. 2016. *Time domain simulation of side-by-side floating bodies using a 3D numerical wave tank approach*. Applied Ocean Research, 58, 189-217.
  43. SHIH, T.-H., LIOU, W.-W., SHABBIR, A., YANG, Z. & ZHU, J. 1995. *A new k-epsilon eddy viscosity model for high reynolds number turbulent flows*. Computers & Fluids, 24, 227-238.
  44. SIMONSEN, C. D., OTZEN, J. F., JONCQUEZ, S. & STERN, F. 2013. *EFD and CFD for KCS heaving and pitching in regular head waves*. Journal of Marine Science and Technology, 18, 435-459.
  45. STERN, F., WILSON, R. & SHAO, J. 2006. *Quantitative V&V of CFD simulations and certification of CFD codes*. International journal for numerical methods in fluids, 50, 1335-1355.
  46. STERN, F., WILSON, R. V., COLEMAN, H. W. & PATERSON, E. G. 2001. *Comprehensive approach to verification and validation of CFD simulations-Part 1: methodology and procedures*. Transactions-American Society of Mechanical Engineers Journal of Fluids Engineering, 123, 793-802.
  47. SUN, L., TAYLOR, R. E. & TAYLOR, P. H. 2010. *First-and second-order analysis of resonant waves between adjacent barges*. Journal of Fluids and Structures, 26, 954-978.
  48. TAN, L., TANG, G.-Q., ZHOU, Z.-B., CHENG, L., CHEN, X. & LU, L. 2017. *Theoretical and numerical investigations of wave resonance between two floating bodies in close proximity*. Journal of Hydrodynamics, 29, 805-816.
  49. TEZDOGAN, T., DEMIREL, Y. K., INCECIK, A. & TURAN, O. 2014b. *Hydrodynamics of heaving twin cylinders in a free surface using an unsteady-RANS method*. The 2nd International Conference on Maritime Technology (ICMT2014).
  50. TEZDOGAN, T., INCECIK, A. & TURAN, O. 2014a. *Operability assessment of high speed passenger ships based on human comfort criteria*. Ocean Engineering, 89, 32-52.
  51. WANG, S., MA, S. & DUAN, W. 2018. *Seakeeping optimization of trimaran outrigger layout based on NSGA-II*. Applied Ocean Research, 78, 110-122.
  52. WANG, X.-L., HU, J.-J., GU, X.-K., GENG, Y.-C. & XU, C. 2011. *Comparative Studies of the Transverse Structure Design Wave Loads for a Trimaran by Model Tests and Rule Calculations [J]*. Journal of Ship Mechanics, 3.
  53. WILCOX, D. C. 1993. *Turbulence modeling for CFD*, DCW industries La Canada, CA.
  54. WU, C.-S., ZHOU, D.-C., GAO, L. & MIAO, Q.-M. 2011. *CFD computation of ship motions and added resistance for a high speed trimaran in regular head waves*. International journal of naval architecture and ocean engineering, 3, 105-110.

55. YASUKAWA, H. 2005. *Influence of Outrigger Position on the Performances of a High Speed Trimaran, . Second Report: Wave-Induced Motions in Head Sea*. Japan Society of Naval Architects and Ocean Engineers, 189-195: Japan Society of Naval Architects and Ocean Engineers.